LBL-34000
UC-406
Preprint

Lawrence Berkeley Laboratory
UNIVERSITY OF CALIFORNIA

Engineering Division

Submitted to Applied Optics

The Relationship between Image Quality and Radiation Dose in Low Energy X-Ray Absorption Tomography

J. Llacer and M. R. Howells

June 1993

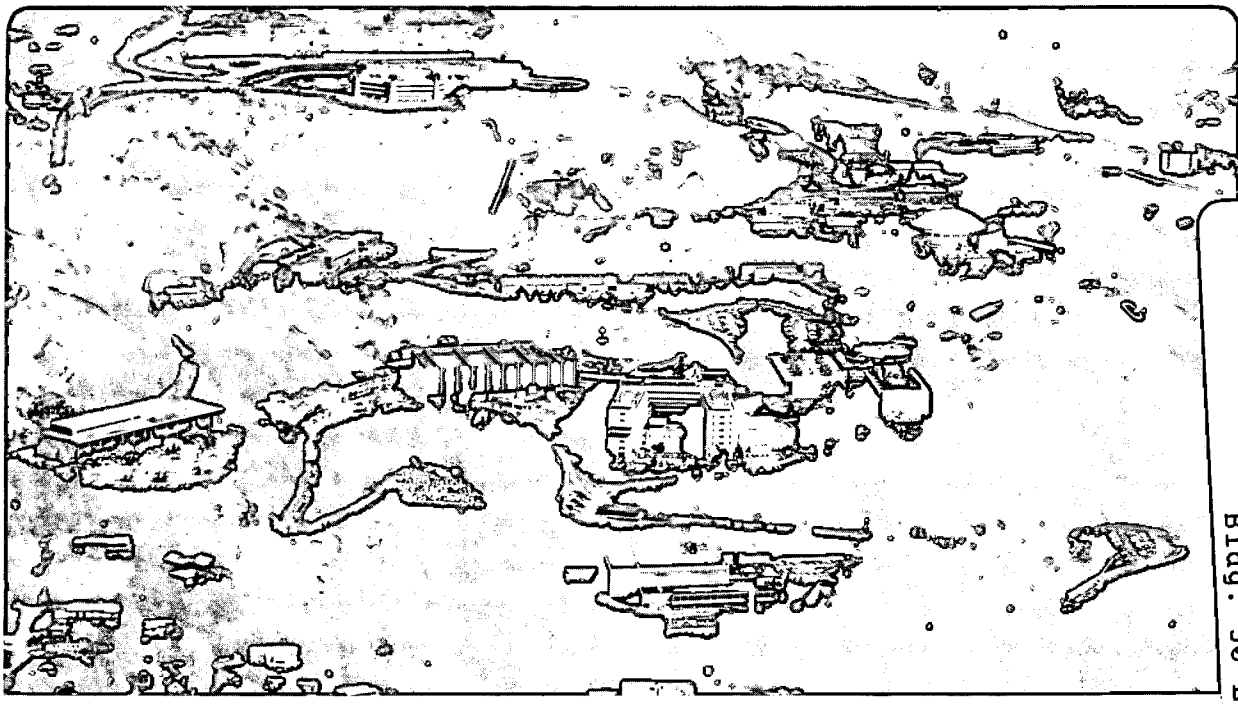

REFERENCE COPY
Does Not
Circulate
Bldg. 50 Library.
LBL-34000
Copy 1

Prepared for the U.S. Department of Energy under Contract Number DE-AC03-76SF00098

DISCLAIMER

This document was prepared as an account of work sponsored by the United States Government. Neither the United States Government nor any agency thereof, nor The Regents of the University of California, nor any of their employees, makes any warranty, express or implied, or assumes any legal liability or responsibility for the accuracy, completeness, or usefulness of any information, apparatus, product, or process disclosed, or represents that its use would not infringe privately owned rights. Reference herein to any specific commercial product, process, or service by its trade name, trademark, manufacturer, or otherwise, does not necessarily constitute or imply its endorsement, recommendation, or favoring by the United States Government or any agency thereof, or The Regents of the University of California. The views and opinions of authors expressed herein do not necessarily state or reflect those of the United States Government or any agency thereof or The Regents of the University of California and shall not be used for advertising or product endorsement purposes.

Lawrence Berkeley Laboratory is an equal opportunity employer.

DISCLAIMER

This document was prepared as an account of work sponsored by the United States Government. While this document is believed to contain correct information, neither the United States Government nor any agency thereof, nor the Regents of the University of California, nor any of their employees, makes any warranty, express or implied, or assumes any legal responsibility for the accuracy, completeness, or usefulness of any information, apparatus, product, or process disclosed, or represents that its use would not infringe privately owned rights. Reference herein to any specific commercial product, process, or service by its trade name, trademark, manufacturer, or otherwise, does not necessarily constitute or imply its endorsement, recommendation, or favoring by the United States Government or any agency thereof, or the Regents of the University of California. The views and opinions of authors expressed herein do not necessarily state or reflect those of the United States Government or any agency thereof or the Regents of the University of California.

LBL-34000
UC-406

THE RELATIONSHIP BETWEEN IMAGE QUALITY AND RADIATION DOSE IN LOW ENERGY X-RAY ABSORPTION TOMOGRAPHY

JORGE LLACER

ENGINEERING DIVISION
Lawrence Berkeley Laboratory
University of California
Berkeley, CA 94720

and

MALCOLM R. HOWELLS

ADVANCED LIGHT SOURCE
Lawrence Berkeley Laboratory
University of California
Berkeley, CA 94720

JUNE 1993

This work was supported by the Director, Office of Energy Research, Office of Health and Environmental Research, Physical and Technological Division, of the U.S. Department of Energy under Contract No. DE-AC03-76SF00098.

recycled paper

LBL-34000

The relationship between image quality and radiation dose in low energy X-ray absorption tomography.

Jorge Llacer, Engineering Division and
Malcolm R. Howells, Advanced Light Source
Lawrence Berkeley Laboratory
University of California
Berkeley, California

Abstract

In this paper we examine the relationship between image quality, defined as the suitability of an image for carrying out a specific task, and the radiation dose needed to obtain that image, for the case of tomographic imaging with low energy X-ray beams of high intensity. The dependence of image quality on the method of tomographic reconstruction for a given dose is specifically addressed. The examples chosen are simulations from the field of biology, but the applicability of the work presented is much wider in scope. The specific tasks that we have selected are the detection and shape determination of thin fibers of protein in water (high contrast case) and the detection and shape determination of cylindrical objects having absorption coefficients substantially lower than protein (low contrast case). The emphasis in current literature to relate Signal-to-Noise (S/N) ratios to dose is demonstrated to be misleading, as that parameter is only one of the factors that may influence the suitability of an imaging method to generate useful results. In the absence of a general, reliable and objective analytical method for predicting human response in evaluating images, we have taken a practical approach and shown reconstructions by rendering then in 3-dimensions, giving our interpretations of the results. S/N ratios have only been used for the purpose of validating the simulation and reconstruction methodology, by comparing simulation results to theoretical calculations. It is shown that simple superposition or Backprojection (BP) of 2-dimensional projections, although yielding excellent S/N ratios, results in images with serious quantitative and qualitative limitations. Filtered Backprojection methods (FBP) with the standard, full resolution ramp filter and with a lower noise Butterworth filter have also been investigated. Both FBP methods result in quantitatively correct images, although they are noisier than the simpler BP images. Finally, we investigate the Maximum Likelihood Estimator (MLE)

method and show that, for the tasks chosen and a given dose, it yields quantitatively correct images and the best detectability of shapes. The dose remains, unfortunately, very high.

1. INTRODUCTION

With the advent of a number of facilities that can generate intense beams of low energy X-rays, the possibility of 3-dimensional tomographic reconstruction at the sub-micron level is being studied at a number of institutions. That possibility would be particularly interesting in the field of Biology, where there is a gap in imaging capabilities between the 10-nm scale of the nucleosome and the micrometer scale of the chromosome[1,2,3]. The wavelengths available from the X-ray facilities would open up that field of imaging, if the necessary absorption or scattering data needed for 3-dimensional tomographic reconstruction can be obtained at a dose to the biological structures that does not progressively destroy them in the process.

It can be expected that the modality chosen for data acquisition method, absorption for tomographic reconstruction or scattering for holography, would have an impact on the minimum dose required to obtain usable images and, likewise, the method of reconstruction can be expected to affect that minimum dose. A number of estimations of dose requirements as a function of irradiation modality have appeared in the literature in the last few years but the effect of tomographic reconstruction method on minimum dose appears to have been studied much less frequently. Nugent and Trebes[4] have examined the case of tomographic reconstruction of multiple views obtained from an X-ray laser modelled as an incoherent source. Poisson noise limited detection is assumed. They propose reconstruction by simple superposition of the projection data onto the image space. In holography this method can be called backpropagation and in absorption tomography it is customarily called backprojection (BP). For the case that those authors have studied, they arrive at the very attractive proposition that simple BP will result in a S/N ratio for the 3-dimensional reconstruction that is given by the square root of the total number of photons scattered by each voxel in the complete process of 3-d data acquisition. The implication of that result is that, if a 2-d projection is useful at a particular S/N ratio which can be obtained with a particular dose D_{2d}, a 3-d reconstruction of similar S/N ratio can be obtained with a total dose of $D_{3d} = D_{2d}$. The dose for each individual projection only needs to be D_{2d} / n_θ, where n_θ is the number of 2-d projections used in the reconstruction.

Unfortunately, the above argument is an oversimplification of the reconstruction problem, as will be shown below. Simple BP yields images that suffer from a number of

qualitative and quantitative drawbacks. They can be useful in some specific cases, but, in general, a more elaborate reconstruction process will be required. In addition, S/N ratios are generally inadequate to determine the usefulness of an image, particularly when attempting to predict the dose required to carry out a particular task. A number of figures of merit or confidence factors have been devised for the purpose of predicting the performance of human observers in carrying out well specified tasks under controlled conditions. However, prediction of success in the task of detection and shape determination of unknown objects in 3-dimensions is still a largely unsolved problem. So far the only statistically meaningful way of evaluating an imaging modality/reconstruction method in relation to human observers is by the well established Receiver Operating Characteristics (ROC) methodology[5]. That procedure has been used recently by Llacer et al.[6] to demonstrate the superiority of Maximum Likelihood Estimator (MLE) methods of reconstruction over Filtered Backprojection (FBP) in medical Emission Tomography. ROC analysis requires extensive tests with human observers and is beyond the objectives of the present work.

This paper focuses its attention on computer simulation of absorption tomography, and reconstruction by simple BP, FBP with the standard ramp and a Butterworth filter, and the MLE method. It is expected that the general conclusions reached will also be applicable to diffraction tomography, although specific numbers will change. The X-ray energy has been chosen so that we operate in the "water window", where absorption by water is minimal, and just above the energy of the C absorption edge, so that protein presents a high absorption coefficient. First, we validate our computer simulations of the absorption process by comparing S/N ratios obtained from those simulations with theoretical S/N ratios in a simple configuration. We specify two tasks, the first of which can be associated with the problem of detecting fibers of supercoiled DNA in water (high contrast) and the second being more generically described as detecting larger objects of low contrast in water. We present the resulting 3-dimensional images through the process of rendering. Only image voxels that have an absorption coefficient above a certain threshold are displayed as a grey level different from background. Voxels below that threshold are rendered as transparent. With this method, it has been possible to carry out comparative evaluations between the different reconstruction methods and arrive at a set of conclusions that, most likely, would be generally accepted by a reader as his/her own. A summary of the notation used in this paper is given as Appendix I.

2. METHODS

2.1 Description of simulated objects and X-ray beams.

We have postulated a perfect X-ray beam of energy 300 eV (λ = 4.132 nm), just above the energy of the C absorption edge, in the water window. The cross section of the beam is $\Delta z \cdot \Delta z$ = 5 x 5 nm and it remains fixed as it traverses the sample. The incident flux density integrated over a fixed measurement time is a variable defined by ϕ photons per nm2. The total flux in the beam is designated by $\phi_0 = \Delta z^2 \phi = 25\phi$ in our simulations. The absorption coefficients used are[7]:

$$\mu_{water} = 4.5 \times 10^{-4}\ (\text{nm})^{-1},$$
$$\mu_{protein} = 7 \times 10^{-3}\ (\text{nm})^{-1}.$$

It is assumed that the length of time that the beam spends in each one of the scan positions is determined by a clock. Then, the actual flux entering the sample is a Poisson variable with a known mean value ϕ. If we could count the entrance beam photons exactly and the beam would move to the next scan position when the desired exact number of photons had been counted, then ϕ would be a deterministic value, but that is not a feasible experimental situation.

We have examined two different simulated objects:

a) Water phantom for validation by theoretical S/N ratios.

Figure 1 shows a uniform water cylinder of diameter 1280 nm and 50 nm height (height not to scale in the figure) divided into 10 horizontal image planes of 128 x 128 voxels, each voxel of dimensions $(\Delta x, \Delta y, \Delta z)$ = (10, 10, 5) nm. The voxel width is twice the beam width for reasons that will be explained later (Section 2.5a). The sample is assumed to rotate over n_θ different angles in the interval $0 \le \theta < \pi$ around the vertical axis of symmetry. For each angle the beam scans the sample along the y-axis at the z-coordinate corresponding to the first horizontal plane, for example. Once the first plane has been scanned at all angles, the process is repeated for the second plane and so on, until all the planes have been scanned. This is the general geometry of all our reconstruction tests.

b) Water cell with protein fibers and lower contrast objects.

Figure 2 shows an elliptical cylinder water cell divided into the same 10 planes as in Fig. 1. There are 15 vertical protein fibers of circular and elliptical cross section ranging in diameter between 20 and 50 nm. In addition there are two regions of elliptical cross section with major axes of 140 and 160 nm and absorption coefficients of 1.45×10^{-3} and 2.45×10^{-3} $(nm)^{-1}$. These regions have low contrast compared to protein which has an absorption coefficient of 7×10^{-3} $(nm)^{-1}$. The different fibers and regions have been placed at random in the water cell. The distribution of the different absorption regions can be seen from the top plane in Figure 2. The fraction of photons absorbed from the incident beam in traversing the water alone along a diameter line is 20%, while traversing the densest part of the simulated object results in an absorption of up to 60%, although this only occurs in some isolated angles θ and beam positions along the z axis.

2.2 Simulated data acquisition.

We have assumed that the parallel X-ray beam enters the sample in a direction perpendicular to the symmetry axis of the cylinder. The beam is assumed to be scanned along the y-axis over 384 positions, covering a distance equal to the length of a diagonal of the square imaging region. The sample is rotated about the symmetry axis over $n_\theta = 256$ evenly distributed angles $0 \leq \theta < \pi$. The size of the beam, scan step size and the number of angles have been chosen so that the conditions described by Huesman[8] to prevent image deterioration due to inadequate sampling are met.

For the validation measurements with the simple water phantom, 20 statistically independent data sets of one sample plane have been simulated. The reconstruction of the independent data sets allows the pixel-by-pixel estimation of S/N ratio, even in the case where adjacent pixels in a particular image are correlated due to filtering, for example.

For the water and protein phantom, 10 statistically independent scans have been simulated from one plane of the phantom. This is equivalent to scanning the complete phantom of Fig. 2 in the ten planes in the z-direction. This will allow a 3-dimensional representation of the reconstructed data.

The total beam flux integrated over the measurement time for one scan position, ϕ_0, is the variable of interest in the simulations. For the validation procedure we have used $\phi_0 =$ 5000 photons. For the water and protein reconstruction experiments, values of $\phi_0 = 50$, 10, 5 and 2.5 photons have been investigated.

2.3 Projection simulation.

Once the map of absorption coefficients for a particular phantom has been generated, as in Figs. 1 and 2, and a flux ϕ_0 has been defined, the mean number of photons being counted by a perfect detector at position j, after the X-ray beam passes through the phantom, is given by

$$\phi_j = \phi_0 e^{-\sum_i \mu_i d_{ji}} \qquad (1)$$

where j ranges over all the scan positions and angles and μ_i is the absorption coefficient of voxel i in the map. The matrix element d_{ji} defines the average length of the intersection between voxel i and a beam j. The matrix **d** is very sparse. The data to be reconstructed are then formed from the mean values given by (1) by using a random number generator to obtain a new set of variables ϕ_{Pj} which are Poisson distributed integers with the corresponding ϕ_j as means. Figure 3a shows a "sinogram" of the noise-free ϕ_j data for one instance of the water and protein phantom corresponding to $\phi_0 = 5$ and Fig. 3b shows the corresponding ϕ_{Pj} data. A sinogram is a compact representation of all the projections obtained from scanning one horizontal plane of an object. Each row of the sinogram contains the 384 bins of the projection for a given angle. The 256 different rows correspond to the different successive scan angles. The data set obtained from scanning the complete three-dimensional object of Fig. 2, for example, would consist of 10 statistically independent sinograms like that of Fig. 3b.

The final step in the simulation consists in converting the sinograms of ϕ_{Pj} to an estimate of mean absorption coefficient $\overline{\mu}_j$ along a beam path j from

$$\overline{\mu}_j L = -\log\left(\phi_{Pj} / \overline{\phi}_0\right) \qquad (2)$$

where L is the length of a beam path and $\overline{\phi}_0$ is an estimate of ϕ_0. In our case, we know the correct value of ϕ_0, but we will instead use an estimate $\overline{\phi}_0$ obtained by finding the average transmitted beam at the edges of the sinogram, where there is no absorption. This is the method that would be used in a real measurement.

2.4. Reconstruction methods.

The reconstruction problem consists in solving for the values μ_i in

$$\bar{\mu}_j L = \sum_i \mu_i d_{ji} . \tag{3}$$

The different methods used to reconstruct the absorption data generated in our simulations will now be discussed.

Backprojection (BP): The simplest reconstruction method consists in backprojecting the values $\bar{\mu}_j$ onto all voxels i of the image plane traversed by the beam j, with weights defined by d_{ji} / L. In a noise-free case, this method results in an image that consists of the original absorption coefficients convolved with the 1/r response of the tomography problem. If the absorption map contains mostly points, as in the phantom of Fig. 2, it is possible to obtain a substantial amount of qualitative information from a BP reconstruction. For example, Fig. 4a) shows the MLE reconstruction (to be described below) of one plane of the phantom of Fig. 2 for ϕ_0 = 50 photons and Fig. 4b) shows the corresponding BP reconstruction. In Fig. 4c) we show a profile along the horizontal line indicated in b) for the MLE reconstruction and in Fig. 4d) we show the corresponding profile for the BP case. All the protein fibers and larger low contrast objects are identifiable in both reconstructions, although the profile for the BP reconstruction clearly shows the effects of the convolution with 1/r. The relative absorption coefficients of the fiber and of the larger object are distorted and the absorption coefficient of water appears different at different image locations. BP reconstructions exhibit an excellent S/N ratio, as will be discussed below, but are often useless because a) one cannot obtain quantitative information from them and b) the effect of the 1/r convolution on absorption or emission maps of complex, low contrast objects often renders the images illegible. In medical tomography, for example, BP reconstructions are never used. Figure 5a shows a positron emission tomography (PET) image of a human brain reconstructed by FBP, Fig. 5b shows the same data reconstructed by the the MLE method (both to be described below) and Fig. 5c) shows the data reconstructed by the simple BP method. In the latter, all grey matter structures have been lost.

Filtered Backprojection (FBP): If one can assume that the point response function (PRF) of the system described by the matrix **d** of (1) is space invariant and the sampling is adequate to prevent aliasing, Fourier methods offer the most common way of reconstructing images obtained from line integrals of absorption coefficients. The effect of

the 1/r response function is effectively removed by convolving each row of $\overline{\mu}_j$ corresponding to a single angle θ with a kernel that, in frequency domain, has the shape |f| up to a cut-off frequency which depends on the sampling frequency of the system. The filtered data are subsequently backprojected into the image plane. Many variations on the |f| filter are in use, mostly for the purpose of "rolling-off" the response function smoothly as |f| approaches the sampling frequency and enhancing some measure of the S/N ratio in the images. The determination of the optimal filter shape is still somewhat arbitrary and depends, mostly, on direct observation of the images by the final users (M.D.'s in medical tomography), guided by spectral analysis of typical images and of the noise. In this paper we shall use both the basic |f| filter and a Butterworth filter that has given excellent results in PET images[9], without claims to optimality.

Absorption image FBP: The beam transmission data of (1) are customarily processed as indicated by (2) in order to obtain an estimate of the absorption map as a result of the reconstruction. For cases with very low flux ϕ_0, an integer Poisson sample ϕ_{Pj} with a mean ϕ_j may be zero. In that case the line integral absorption coefficient $\overline{\mu}_j$ of (2) goes to infinity and the FBP reconstruction cannot be carried out. We have found, however, that in those cases, it is possible to reconstruct for the number of photons absorbed by a pixel instead of reconstructing for the absorption coefficient. A new set of data is generated by

$$\phi_{aj} = \phi_{Pj} - \overline{\phi}_0 \tag{4}$$

which consists of the difference between the measured transmitted counts and the estimated initial beam flux. ϕ_{aj} is an estimate of the number of photons absorbed along the beam path. Once the FBP reconstruction has been completed, the results can be converted to absorption coefficient, if desired. This method can be expected to work for the case in which it can be assumed that the average number of photons absorbed while the beam traverses the sample is small compared to the initial flux ϕ_0, i.e., the probability of a photon being absorbed at a pixel depends mainly on the absorption coefficient of that pixel, and not of its position along the beam direction. The parameters used for the phantoms of Figs. 1 and 2 fulfill that requirement approximately. As indicated above, the average number of photons absorbed from the beam in traversing the water aslong a diameter line of the simulated objects is approximately 20%. If we re-design the experiment to make measurements for $0 \le \theta \le 2\pi$, i.e., we irradiate from both ends of each beam direction, with half the flux from each direction, the maximum absorption is reduced to approximately 5%. The re-designed experiment does not affect the results of our simulations. It only

makes reconstruction by FBP plausible for the cases with low photon counts. The absorption image FBP method has been needed for the reconstructions with fluxes ϕ_0 = 12.5, 5 and 2.5 photons.

Maximum Likelihood Estimator (MLE): The MLE method of image reconstruction is a non-linear method based on statistical parameter estimation. Its characteristics and benefits have been studied over the last several years principally for emission tomography, both single photon (SPECT) and positron emission (PET). The principal distinguising characteristic of MLE reconstructions in PET is that the expected error in a reconstructed pixel is approximately proportional to the square root of the intensity of the pixel. On the other hand, FBP reconstructions of equal resolution yield an expected error that is largely independent of the intensity and is as high as the higher expected errors in the MLE[9]. The MLE method yields images in which detectability of small objects brighter than the background in the neighborhood of large bright objects is enhanced substantially[10].

A version of MLE for X-ray absorption has been published by Lange and Carson[11]. Because of the decreasing number of photons in the beam as it traverses the sample, the algorithm is relatively complex and has to resort to some approximations. However, for the case considered in this paper in which the absorption image approximation described in the previous section can be expected to hold, it is possible to use the same algorithm that has been developed for PET with the only effect being that the resulting image corresponds to absorbed photons, just as in the case of FBP with low flux.

The MLE is an iterative method that has to be stopped according to a well defined statistical test for consistency. Ref. 9 describes in detail the MLE for PET, which, with minor modifications has been used for the work described in this paper.

2.5. Calculation of S/N ratio.

There are two methods in the literature for the calculation of S/N ratio in the case of a uniform circular absorber: the one resulting from the work of Huesman[8] and that of Barrett and Swindell[12]. We shall describe the two methods in the context of our application.

a) Huesman's method.

Huesman described the effect of projection bin size (beam width) and number of projection angles on average S/N ratio for a uniform circular absorber in FBP reconstructions with the basic |f| filter (ramp filter). For a bin size $\Delta z \leq 0.5\ \Delta x$ (where Δx is the voxel lateral dimension, $\Delta x = \Delta y$) and for a number of angles $n_\theta \geq 1.5\ D/\Delta x$, where

D is the diameter of the absorber, he found that S/N is at its best. For our phantom, $D = L$, the beam path length. The above conditions are fulfilled by the parameters of our simulations. S/N ratio in a reconstruction is defined as the average voxel value over an ensemble of reconstructions from independent data sets of the same object divided by the standard deviation of that voxel value over the ensemble. The S/N ratio of a projection is defined similarly over projection bins instead of voxel values.

Under the optimum conditions indicated above, the relationship between S/N ratio in the line integral absorption coefficients of a single projection and the S/N ratio of the tomographic reconstructions is given by

$$\left(\frac{S}{N}\right)_{rec} = \left(n_\theta n_z \frac{\Delta x^3}{D^3}\right)^{1/2} \left(\frac{S}{N}\right)_{proj} \tag{5}$$

where n_z is the number of bins in one projection angle. For the conditions of our simulation, (5) results in

$$\left(\frac{S}{N}\right)_{rec} = 0.177\left(\frac{S}{N}\right)_{proj}. \tag{6}$$

A tomographic measurement yields the number of transmitted photons and the S/N ratio in transmitted photons can be calculated from those measurement. However, in order to use (5) or (6), we have to calculate the S/N ratio in the projection data as line integral of absorption coefficients. In order to do that we note that, as before, ϕ_j is the average number of photons reaching the projection plane for a particular beam position j and so $\sigma_{\phi j} = \sqrt{\phi_j}$ is the corresponding standard deviation. Then, with the initial flux ϕ_0 define as above,

$$\log\left(\frac{\phi_j \pm \sigma_{\phi j}}{\phi_0}\right) = \log\left(\frac{\phi_j}{\phi_0}\right) \pm \log\left(1 + \frac{\sigma_{\phi j}}{\phi_j}\right) \approx \log\left(\frac{\phi_j}{\phi_0}\right) \pm \frac{\sigma_{\phi j}}{\phi_j} \tag{7}$$

for reasonably good S/N ratio in the projection. Then we can rewrite the r.h.s expression of (7) using the average absorption coefficient over a path $\overline{\mu}_j$ and its standard deviation $\sigma_{\overline{\mu} j}$. Thus

$$\log\left(\frac{\phi_j}{\phi_0}\right) \pm \frac{\sigma_{\phi j}}{\phi_j} = \left(\overline{\mu}_j \mp \sigma_{\overline{\mu} j}\right)L. \tag{8}$$

Then, the S/N expression in absorption coefficient for a single projection is

$$\left(\frac{S}{N}\right)_{proj} = \frac{\left|\log\left(\frac{\phi_j}{\phi_0}\right)\right|}{\left(\frac{\sigma_{\phi j}}{\phi_j}\right)} \quad (9)$$

This is a number calculated from our knowledge of the simulated objects which can be used in conjunction with (5) or (6) to calculate the final S/N ratio that Huesman predicts the FBP algorithm should deliver in the reconstructed pixels. Huesman developed (5) for the average S/N ratio over the whole image, but we shall not consider the relatively small differences between average and central S/N ratios.

b) Barrett and Swindell's method.

Those workers have developed a very complete theory of S/N ratio resulting from FBP reconstructions, which, for the case of a uniform circular object of absorption coefficient μ and a ramp filter yields a simple expression for the S/N ratio at the center of the absorber. Their result is

$$\left(\frac{S}{N}\right)_{rec} = 0.665\mu\delta^{3/2}\left(n_\theta\phi_0 e^{-\mu D}\right)^{1/2} \quad (10)$$

where the resolution figure $\delta = 0.7 / f_{\max}$ is related to the cutoff frequency of a filter with an abrupt cutoff and in our case with Δz= 5 nm and the Nyquist frequency as the cutoff, would be equal to 7.0 .

Eqs. (9) and (10) will be used below to validate our simulations in terms of calculated vs. measured S/N ratios in reconstructions of the phantom of Fig. 1.

2.6. Calculation of radiation dose.

The aim of this calculation is to determine the dose in ergs/gm absorbed by one pixel of a phantom with local density ρ and absorption coefficient μ. Specifically, we consider the case in which a pixel is irradiated from many directions, as in a tomographic measurement. We begin by replacing a pixel of side dimension d by a circle of equivalent area, with diameter

$$d' = \frac{2d}{\sqrt{\pi}}. \tag{11}$$

The mean path length of beams traversing the circle is

$$L = \frac{\pi d'}{4} \tag{12}$$

and the number of beam widths traversing the circle of diameter d' is

$$W = \frac{d'}{\Delta z} \tag{13}$$

with Δz being the beam width. The total flux traversing the circle is, then,

$$\phi_{tot} = \phi_0 W n_\theta \tag{14}$$

with n_θ being the number of projection angles taken. According to Section 2.1,

$$\phi = \frac{\phi_0}{\Delta z^2}. \tag{15}$$

The total number of photons absorbed by the pixel is then given by (11) - (15) as

$$\Delta\phi \cong \phi_{tot}\mu L = \mu\phi\Delta z n_\theta d^2. \tag{17}$$

Let ε be the energy of a photon in eV. Then the energy deposited in a pixel will be $\Delta\phi\varepsilon \times 1.602 \times 10^{-12}$ ergs. For a beam of square cross section Δz x Δz, the mass of the pixel is $d^2\Delta z\rho$ and the final dose expression is

$$\text{Dose} = \frac{\mu\phi\varepsilon n_\theta \times 1.602 \times 10^{-12}}{\rho} \text{ (ergs/gm)} \tag{18}$$

where μ is in (cm)$^{-1}$, ϕ is in (cm)$^{-2}$, ε in eV and ρ in gm /(cm)^3. The value of ρ for "generic" protein has been taken to be 1.35[13] . There is a worst-case assumption in this calculation, which assumes that every pixel is illuminated by the entire incident beam, i.e., a weak absorption approximation has been made, just as in some of the reconstruction procedures.

3. VALIDATION OF SIMULATION PROCEDURE

The computer programs used for the simulation and reconstruction steps are the result of minor changes to programs that have been in use over a number of years for research in emission tomography. Nevertheless, a comprehensive validation is necessary by comparing theoretical to measured results in the present case of absorption tomography.

That validation can be provided by a comparison of the S/N ratios calculated from the theoretical work of Huesman, and Barrett and Swindell with the results of simulating a uniform water absorber, the absorption measurements and reconstructions by FBP.

Twenty statistically independent absorption data sets corresponding to one plane of the phantom of Fig. 1 have been obtained by the methods indicated in the sections 2.2 and 2.3. Equation (1) has been the basis for the simulation followed by the generation of sinograms of Poisson data. A total entrance flux = 5000 photons in the 25 nm^2 cross section of the beam has been used. Prior to reconstruction, the sinograms of transmitted counts were converted to line integrals of absorption coefficients by Eq. (2), with the estimate $\overline{\phi}_0$ obtained from the 8 left-most and 8 right-most projection bins which are empty averaged over the 256 projection angles. The resulting 20 sinograms and corresponding reconstructions by FBP with the ramp filter (|f|) have been analyzed statistically by finding the suitable averages over the ensemble of sinograms and reconstructions. Those averages let to the desired S/N ratios. Table 1 shows the S/N ratios obtained experimentally at the center of the projections and of the reconstructions, compared to the results from calculations following the Huesman and the Barrett and Swindell methods.

The 20 independent data sets have also been reconstructed by the simple backprojection (BP) method and the S/N ratio at the center of the reconstructions has been measured. The results are also shown in Table I.

Table I shows a good agreement between the simulations and analytic calculations of S/N ratios, both in the projections and in the reconstructions. Both Huesman's and Barrett & Swindell's methods give somewhat higher S/N ratios than the measured simulated results. The difference can be due to a number of factors: the continuous approximation to the discrete problem in the analytical treatments, the difference between average S/N ratio and S/N ratio at the center of the image in the case of Huesman's results and, perhaps more importantly, the noise introduced by the linear interpolation used by the backprojection algorithm used in the simulations (Function BIN in the Donner algorithms[14]). The essential points are clear though: the S/N ratio of a single projection data gets considerably reduced by reconstruction by FBP, in good agreement with (6). On the other hand, reconstructing by simple superposition or backprojection (BP) results in a S/N ratio which is approximately equal to the S/N ratio of a single projection multiplied by the square root of the number of projections. This is in good agreement with the conclusions drawn by Nugent and Trebes[4] for simple BP in tomographic image reconstruction of holography data. It follows that, if the quality of images obtained by BP is adequate for a particular

task, the dose for tomographic reconstruction can be reduced in each view by the number of views and obtain the same S/N ratio in the reconstruction as one could obtain by the original dose in one single projection. Unfortunately, image quality in BP reconstructions is not likely to be good for any practical purposes, as suggested earlier. We shall return to this point below.

4. RESULTS WITH THE WATER AND PROTEIN PHANTOM

As indicated in the earlier part of the paper, S/N ratio is only one factor that enters into the evaluation of an imaging method that is to be used for a particular task. In the absence of a general analytical methodology to determine a reliable figure-of-merit to predict the performance of a human observer, except in very simple tasks, we shall take a practical approach in this paper and discuss two specific tasks for which the phantom of Fig. 2 is relatively appropriate: 1) detecting the existence and shape of high contrast protein fibers in a water cylinder and 2) determining the existence and shape of low contrast elliptical cylindrical regions in the same water environment. In order to decide whether a given flux allows the successful performance of tasks 1) and 2), we will use a rendering method to display the 3-dimensional images generated and present our qualitative evaluations of the images. We expect that readers would arrive at the same conclusions. The radiation doses for each of the results will be given as a table.

Since the beam width Δz is half of the pixel side dimension Δx, the sampling distance is such that the Nyquist condition is fulfilled for individual pixels, i.e., the FBP method with the ramp filter will yield the maximum resolution attainable by any linear method of reconstruction. The ramp filter is however very noisy and a Butterworth filter is often used to reduce noise at the expense of some resolution. We use both filters in the work to be reported below. In our implementation of the MLE algorithm, the final resolution falls between those of the ramp and the Butterworth filter, but it results in lower noise than any of the two.

Task 1) Detectability and shape determination of high contrast protein fibers:

Figure 6 shows a three-dimensional rendering of the original protein fibers in the phantom of Fig. 2. The display software allows a range of absorption coefficients to be made transparent. In Fig. 6, the transparency range has been set between 0.0 and 4×10^{-3} $(nm)^{-1}$, effectively making the water and the large elliptical low absorption regions transparent. We call the higher of the two values indicated above the "upper threshold for transparency" and it will play an important role in the description of our results. The

reconstructions always attempt to recover all the objects in the imaging volume. It is only at the time of displayint the results that the 3-dimensional rendering is used with the transparency feature discussed above.

Figure 7a shows the rendering of the reconstruction results by the FBP-ramp method for the case with $\phi_0 = 50$ photons in the X-ray beam. Figure 9b shows the same rendering for the FBP-Butterworth reconstruction and Fig. 9c corresponds to the MLE results. The upper threshold for transparency has been set as low as possible, up to a point in which some noise voxels begin to appear. These thresholds are lower for the reconstructions with lower noise in the water background. In all three cases, however, the fibers can easily be detected and they appear unbroken, although with some irregularities in the noisier reconstructions. As the noise performance of the reconstruction improves allowing the upper transparency threshold to be lowered, voxels with lower absorption coefficient in the FBP-Butterworth and MLE (with lower resolution than the FBP-ramp) are being accepted for rendering on the surface of the fibers and, for that reason, the FBP-Butterworth and MLE renderings appear darker than the FBP-ramp rendering. Also, as the thresholds for transparency are being lowered, the larger low density elliptical regions begin to appear.

The reconstructions for the BP method have been rendered in Fig. 7d. The intensity of a BP image depends not only on the absorption coefficient of an object, but also on its size and location relative to other objects. It is not very clear what the actual size of the fibers is since the apparent thickness in the rendering depends on the setting of the upper threshold for transparency. Also, some objects are lost and only appear when the upper threshold for transparency is lowered substantially. In that case, strong noise appears all over the image. All those effects are due to the convolution with the 1/r intrinsic point response function of the unfiltered tomography process. For those reasons, the upper threshold for transparency has to be tailored to a specific object or set of objects, which can only be done is one knows, a priori, what the size of the object is. We have aimed at rendering the larger diameter fibers near the reader with as good a quality as reasonably possible. Other fibers appear too thin. Notice that the large elliptical low absorption region appears quite promimently because of its large size, altough is has lower absorption coefficient than the thin fibers.

Figures 8a, b, c and d show the reconstructions results for a flux $\phi_0 = 10$, i.e., five times lower than in the previous case. The high resolution MLE-ramp shows a large amount of noise that becomes intrusive when attempting to render the protein fibers. The ramp filter will not be used for fluxes lower than 10. The FBP - Butterworth results are

better and it is possible to set the upper threshold for transparency to a point where most of the fibers can be accounted for, with only a moderate amount of clutter due to noise. Note that the thinnest fiber, partially occluded by a large diameter one near the center of the plane cannot be distinguished from noise clutter. The MLE results are substantially better than the FBP-Butterworth results. The transparency threshold can be placed low enough to show all the fibers in their full dimension, including the one that was missing in the FBP-Butterworth reconstruction, with a similar or lower amount of noise clutter. The rendering of the larger fromt fibers in the BP image is good, although it is not possible to know where the edges are and close fibers are rendered into one. Many other fibers have disappeared.

Figures 9 a and b show the reconstruction by MLE and BP for the case of $\phi_0 = 2.5$, the lowest value investigated. FBP - Butterworth results were useless at this low flux. The MLE results are marginal for the task under study, particularly for the thinnest fibers. We could state that we have arrived at the MLE limit of sensitivity for the task on hand. The BP results show some of the larger fibers well, but the thinner fibers have disappeared. Lowering the transparency threshold brings some of those fibers back, but noise distorts the thick fibers substantially.

It is important to make a comment regarding the rendering of the BP results in all the above reconstructions. Because of the binary nature of the information (there is protein, or there isn't) and the use of a threshold for transparency, the rendered fibers in the BP reconstructions appear sharp. In reality the reconstruction results are far from sharp, as can be seen in the profiles of Fig. 4d, since they are convolved with a 1/r function. Changing the upper threshold level for transparency will always render the fibers sharp but of a diameter that depends on the threshold setting. Accurate shape determination of an imaged object is, therefore, not possible with the BP method.

Task 2) Detectability and shape determination of low contrast objects

The behavior of the different reconstruction methods with regard to the task of observing the low constrast objects has been carried out in a manner similar to the first task. Examination of the rendered reconstructions indicates similar results to the first task, except that the lowest flux at which one can definitely detect the lowest density object with any degree of certainty is at $\phi_0 = 10$ and that is with the MLE or the BP method. Again, the diameter of the rendered large elliptical regions depends on the setting of the transparency threshold in the BP method.

5. CALCULATION OF RADIATION DOSE

Table 2 shows the calculated dose absorbed by the water and generic protein of the phantom of Fig.2, for the different fluxes used in the above simulations. The results have been calculated from Eq. (18) and are given in ergs/gm.

6. DISCUSSION AND CONCLUSIONS

In spite of the excellent S/N ratio for reconstruction of extended uniform objects, as in the phantom of Fig. 1, the simple BP reconstruction method has been shown to yield images that do not have higher effective sensitivity than the MLE method for the two tasks studied. The reason for this is, again, the convolution effect with the 1/r point response function of the tomographic system. The noise in a uniform background in a BP reconstruction is low because of the superposition of noises originating in the different projection data, which tend to average out. Objects with higher absorption coefficient than the background are convolved with the 1/r kernel which makes them spread over the whole image plane. The spatial resolution for the reconstruction is consequently much poorer than that of the projections. At the original location of the objects, the signal magnitude is strongly diluted with respect to the background, so that contrast levels in the reconstruction are low. As indicated above, this method of reconstruction yields a distribution of reconstructed image intentisities that depends not only on the absorption coefficients of the original object, but also shows an erroneous dependence on the size and location of the objects.

The shortcomings of the BP method have dictated the need to deconvolve the 1/r response function from the projection data, with the majority of applications using the FBP method, with a diversity of filters. At equal resolution in positron emittion tomography (PET), it has been shown that a correctly implemented MLE method will have more sensitivity for the types of tasks discussed in this paper than the FBP method[9]. We have shown in this paper that that is also the case in low energy X-ray absorption tomography. The above data support the claim that MLE provides a factor of between 5 and 10 better sensitivity than FBP and that BP, in additioin to its other shortcoming, does not provide a better level of sensitivity than the MLE method.

The doses indicated in Table II are very large and in the absence of a reconstruction method that provides also a very large increase in sensitivity, the possibility of successfully carrying out tomography with biological samples at the sub-cellular level is open to

question. The above results suggest a possible direction to follow in preliminary experiments to study the feasibility of tomographic imaging: repeated single projection imaging experiments in order to study the changes in the samples as a function of dose, coupled to simulation experiments like the ones described in this paper in order to determine the expected quality of obtainable images for the specific task to be carried out.

7. ACKNOWLEDGMENTS.

The authors would like to acknowledge the encouragement of Aloke Chatterjee at the Lawrence Berkeley Laboratory. The work of this paper has been supported by the Director, Office of Energy Research, Office of Health and Environmental Research, Physical and Technological Division, of the U.S. Department of Energy under Contract DE-AC03-765SF00098.

8. BIBLIOGRAPHY

1. *Form and Function, Perpectives on Structural Biology and Resources for the Future"*, U.S. Department of Energy, December 1990.

2. J.W. Gray and J. Trebes, "Cromatin structure and X-ray imaging: Static and dynamic considerations", Proc. of the Workshop on X-Ray Microimaging for the Life Sciences, Lawrence Berkeley Laboratory, May 1989, Report LBL-27660.

3. E.M. Bradbury, "Organization, structure and function of chromosomes", Proc. of the Workshop on X-Ray Microimaging for the Life Sciences, Lawrence Berkeley Laboratory, May 1989, Report LBL-27660.

4. K.A. Nugent and J. E. Trebes, "Signal to Noise ratio and image quality for 3D multiple view X-ray microscopy", University of Melbourne Report UM-P-93/59 (1993), unpublished.

5. C.E. Metz, "ROC Methodology in radiologic imaging", Investigative Radiology, Vol. 21, No. 9, pp. 720-733, 1986.

6. J. Llacer, E. Veklerov, L.R.Baxter, S.T.Grafton, L.K.Griffeth, R.A. Hawkins, C.K. Hoh, J.C. Mazziotta, E. J. Hoffman and C.E. Metz, accepted for publication in The Journal of Nuclear Medicine, 1993.

7. S. Rothman, "New biological science with X-ray microimaging", Proc. of the Workshop on X-Ray Microimaging for the Life Sciences, Lawrence Berkeley Laboratory, May 1989, Report LBL-27660.

8. R.H. Huesman, "The effects of a finite number of projection angles and finite lateral sampling of projections on the propagation of statistical errors in trasverse section reconstruction", Phys. Med. Biol., Vol. 22, No. 3, pp. 511-521, 1977.

9. J. Llacer, E. Veklerov, K.J.Coakley, E. J. Hoffman and J. Nunez, "Statistical analysis of Maximum Likelihood Estimator images of human brain FDG PET studies", to be published in IEEE Trans. Med. Imaging, June 1993.

10. J. Llacer, E. Veklerov, L.R. Baxter, S.T. Grafton, L.K. Griffeth, R.A. Hawkins, C.K. Hoh, J.C. Mazziotta., E.J. Hoffman and C.E. Metz, "Results of a clinical ROC study comparing Filtered Backprojection and Maximum Likelihood Estimator images in FDG PET studies", accepted for publication, Journal of Nuclear Medicine, July 1993.

11. K. Lange and R. Carson, "EM reconstruction algorithms for emission and transmission tomography", J. Comp. Assist. Tomography, No. 8, pp 306-316, 1984.

12. H. H. Barrett and W. Swindell, *Radiological Imaging: the theory of image formation, detection and processing*, pp. 597-603, New York, Academic Press, 1981.

13. R. A. London, "Radiation damage and its influence on source requirements for high resolution X-ray holography", Proc. of the Workshop on X-Ray Microimaging for the Life Sciences, Lawrence Berkeley Laboratory, May 1989, Report LBL-27660.

14. R. H. Huesman, G. T. Gullberg, W. L. Greenberg and T.F. Budinger, "Donner Algorithms for Reconstruction Tomography", Publication 214, Lawrence Berkeley Laboratory.

APPENDIX 1 - NOTATION

d_{ji}	matrix element that defines the average length of intersection between pixel i and beam j.
$\mathbf{d}$	matrix containing the elements d_{ji}.
D	Diameter of a uniform absorber for S/N calculations
i	Index that ranges over all voxels in the sample volume.
j	Index that ranges over all the beam scan positions and rotation angles
L	Length of a beam path
n_θ	Number of scan angles.
n_z	Number of bins in one scan angle.
$\Delta x, \Delta y, \Delta z$	Dimensions of an image voxel, in nm.
$\Delta z \cdot \Delta z$	Cross sectional area of the X-ray beam, in nm^2.
$\Delta\phi$	Total number of photons absorbed by a pixel, in calculation of dose.
ε	Energy of a photong, in eV.
ϕ	Incident X-ray beam flux integrated over a fixed measurement time, in photons per nm^2.
ϕ_0	Total incident flux in the X-ray beam, integrated over a fixed measurement time, in photons.
$\overline{\phi}_0$	Estimate of ϕ_0 obtained from a set of simulated measurements.
ϕ_{aj}	Estimate of the number of photons absorbed along beam path j.
ϕ_j	Mean photon flux of exit X-ray beams after passing through the sample at beam position and angle defined by index j.
ϕ_{Pj}	Poisson distributed integer corresponding to a mean value ϕ_j obtained by a random process.
μ	Local value of absorption coefficient of an object.

μ_i	Absorption coefficient at a voxel i in the sample volume.
$\overline{\mu}_j$	Mean absorption coefficient along a beam path length
ρ	Local value of density of an object
$\sigma_{\overline{\mu}j}$	Standard deviation in absorption coefficient along a beam path length.
θ	Angle of sample rotation about central axis of image plane during sample scanning.

TABLE I

Comparison of theoretical vs. measured S/N ratios in simulations

Flux ϕ_0	Method	S/N Proj. counts	S/N Proj. abs.coeff.	S/N Reconstruction
5000 cts.	Simulation FBP, measured	55.46	*32.14	3.55
	Calculated, Huesman	53.02	30.54	5.39
	Calculated, Barrett & Swindell			4.70
	Simulation, BP, measured			481.05

* Calculated from Equation (9).

TABLE II

Dose absorbed by phantom of Fig. 2.

Parameters: $\mu_{water}=4.5\times10^{-4}(nm)^{-1}$; $\mu_{protein}=7\times10^{-3}(nm)^{-1}$;
$\rho_{water}= 1\times10^{-21}(g/nm^3)$; $\rho_{protein}= 1.35\times10^{-21}(g/cm^3)$
$\varepsilon = 300$ eV
$n_\theta = 256$ angles, fluxes integrated over the measurement time.

Integrated flux ϕ_0 in beam cross-section	Flux density ϕ, in photons per nm^2	Dose to water, ergs/gram	Dose to protein, ergs/gram
50	2.0	1.11×10^{11}	1.27×10^{12}
10	0.4	2.21×10^{10}	2.55×10^{11}
5	0.2	1.11×10^{10}	1.27×10^{11}
2.5	0.1	5.53×10^{9}	6.38×10^{10}

FIGURE CAPTIONS.

Figure 1 - Geometry of the 3-dimensional simulations. The simulated water object was used for verification of our simulation procedures by comparing S/N ratio in 20 independent realizations of one plane of the object with theoretical values. Note that the vertical (Z) direction in this figure, as well as in all the other phantom figures, is not shown to scale.

Figure 2 - Simulated object containing 15 filaments of protein with dimensions ranging between 20 and 50 nm diameter (high contrast) and two larger cylindrical regions of low contrast, all immersed in a water elliptical "cell".

Figure 3 - a) Sinogram of average transmitted beam through the object of Fig. 2, noise free case; b) After Poisson sampling for a time integrated flux $\phi_0 = 5$ photons in the beam cross section. A row in the sinogram corresponds to counts detected in projection at a given angle. There are 256 rows corresponding to the number of scan angles in the simulation.

Figure 4 - a) Maximum Likelihood Estimator (MLE) reconstruction and b) simple backprojection (BP) reconstruction of one plane of the object of Fig. 2, for the case with $\phi_0 = 50$ photons; c) Profile through the line indicated in b) for the MLE results, and d) for the BP results. Notice the effect of the convolution with a $1/r$ kernel in the latter, which makes a large, low contrast object appear brighter than as a small high contrast object.

Figure 5 - a) Filtered backprojection (FBP) reconstruction of a human Fluoro-deoxyglucose Positron Emission (PET) scan at mid brain, and b) MLE reconstruction of the same data compared to c) a Backprojection (BP) reconstruction of the same data. The effect of convolving with the $1/r$ kernel virtually renders the BP reconstruction featureless.

Figure 6 - Rendering of the protein fibers in the object of Fig. 2 - Rendering is done by selecting a region of image densities which will be made transparent in the representation. The remaining image elements are shown as solids with a color in the boundary that depends on the density (absorption coefficient, in this case) of the reconstruction at the particular boundary pixels. By definition, that density has to be above an "upper threshold for transparency".

Figure 7 - Rendering of the reconstruction of protein fibers for the case with a flux $\phi_0 = 50$ photons. a) FBP-ramp filter; b) FBP-Butterworth filter; c) MLE; d) BP. For the first three cases, the upper threshold for transparency has been placed at a density value that yielded images with similar amount of clutter due to noise. In the BP case, we have attempted to place the threshold at a density that allowed for viewing most of the high contrast fibers.

Figure 8 - Rendering of the protein fibers for the case with $\phi_0 = 10$. a) FBP-ramp; b) FBP-Butterworth; c) MLE and d) BP. We have attempted to select a transparency threshold that yielded similar amounts of clutter in the first three images. For the BP reconstruction, we have attempted to insure that the larger fibers near the front were well defined.

Figure 9 - Rendering for $\phi_0 = 2.5$. a) MLE and b) BP. We have attempted to show the thicker fibers near the reader with similar quality in the two cases.

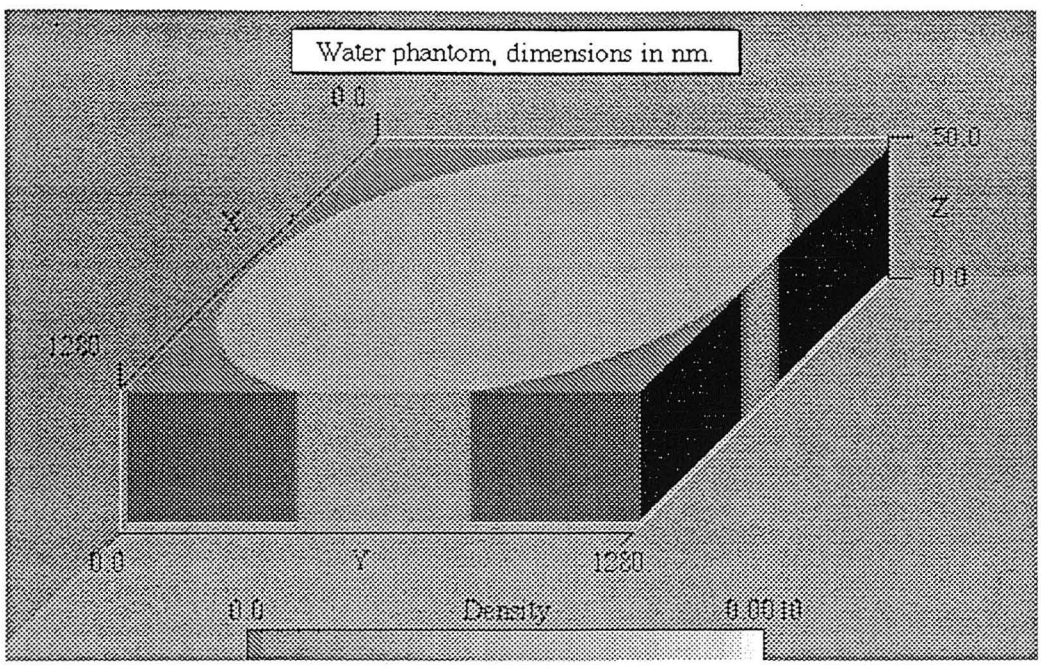

Figure 1

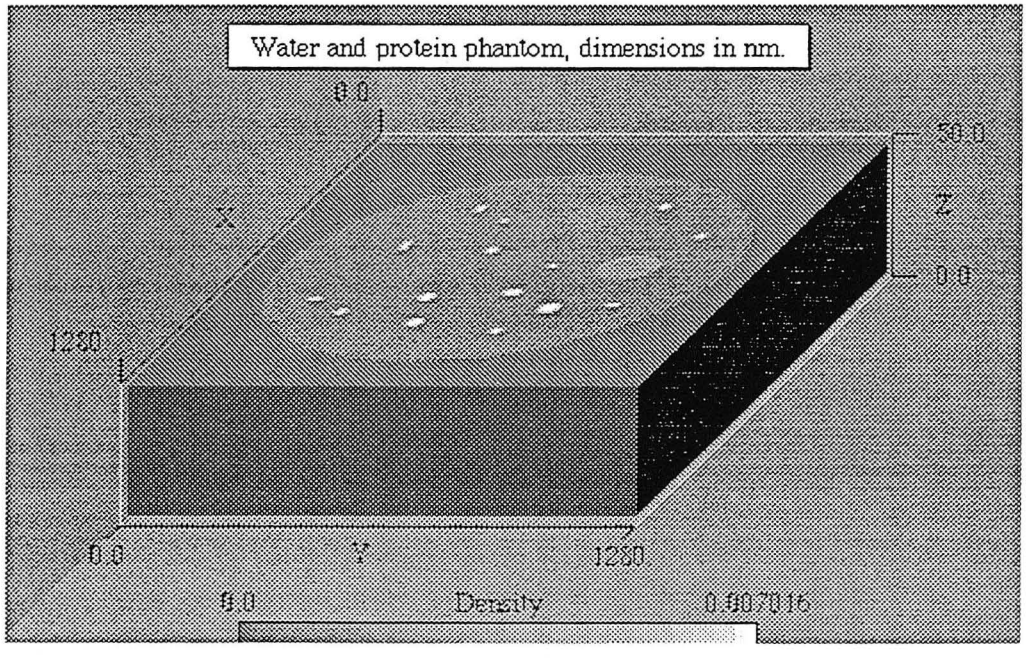

Figure 2

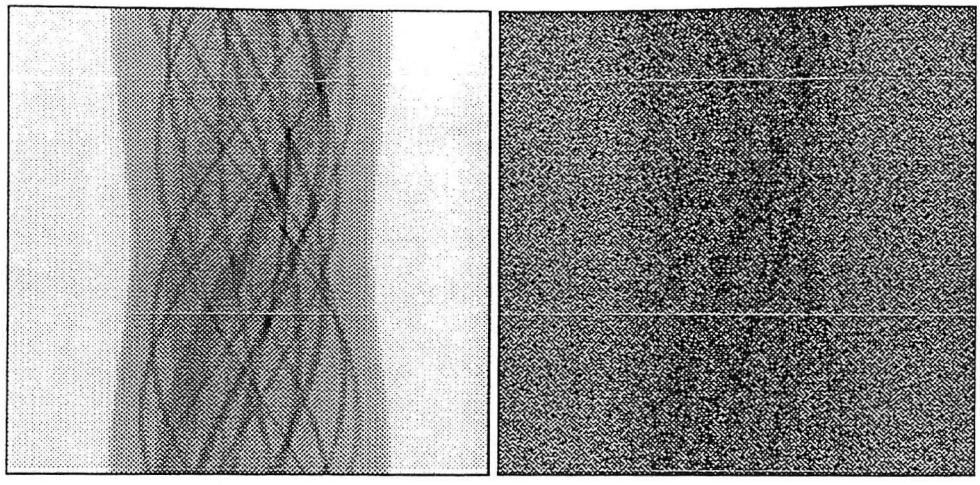

a) Average transmitted beam

b) Poisson sampling

Figure 3

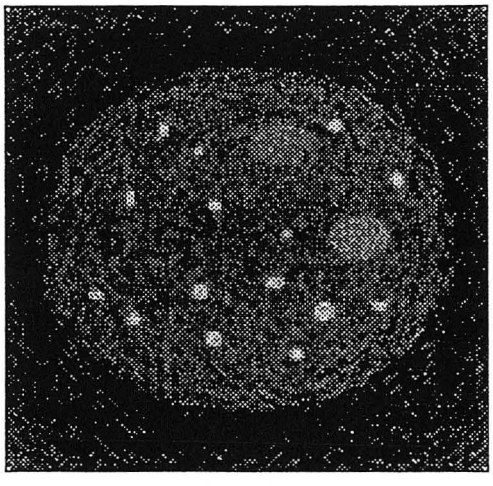

a) Single plane, MLE, Flux = 50

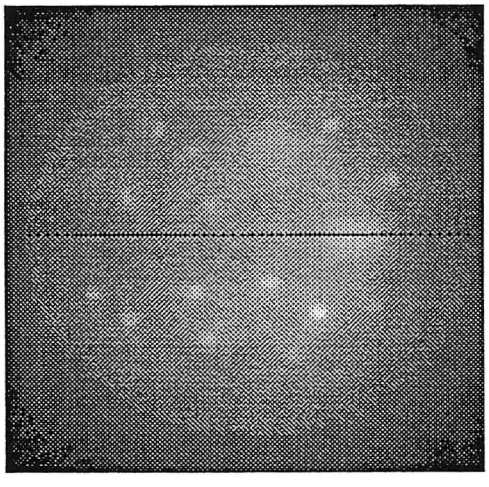

b) ditto, simple backprojection

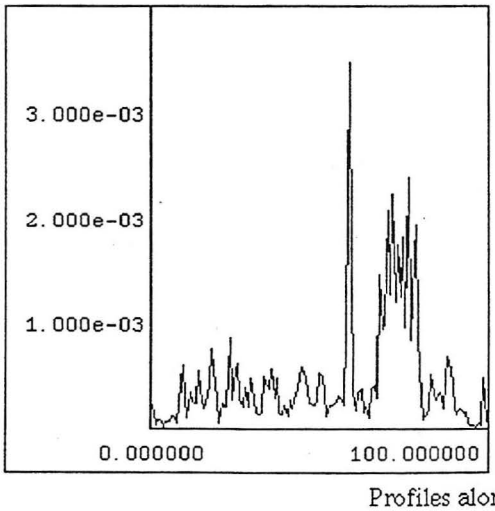

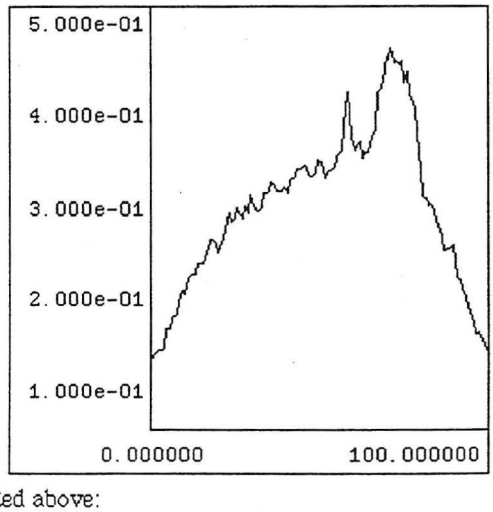

Profiles along line indicated above:

c) for MLE image

d) for backprojection image

Figure 4

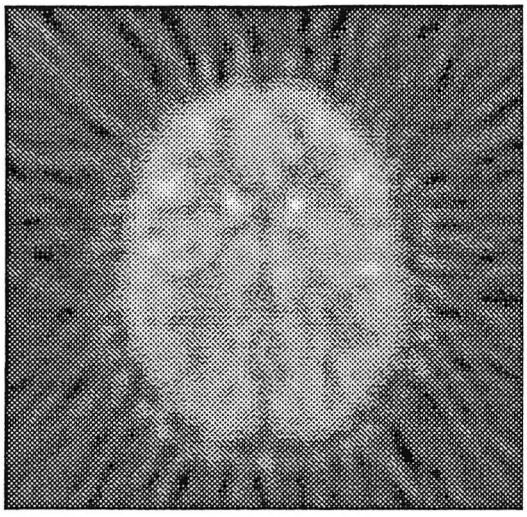

a) Filtered Backprojection

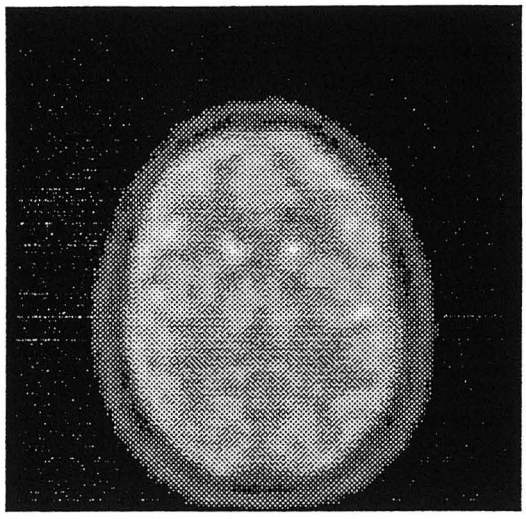

b) Maximum Likelihood Estimator

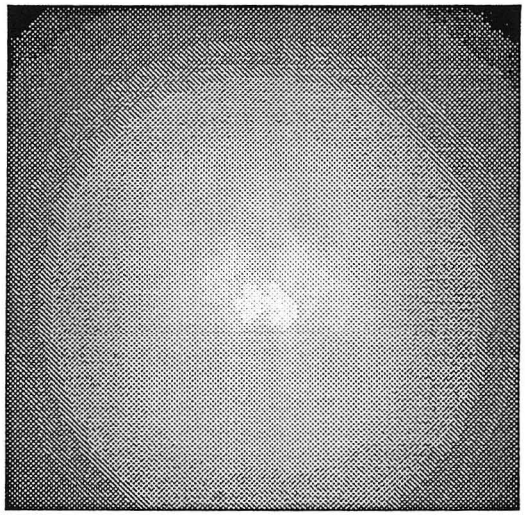

c) Simple Backprojection

Figure 5

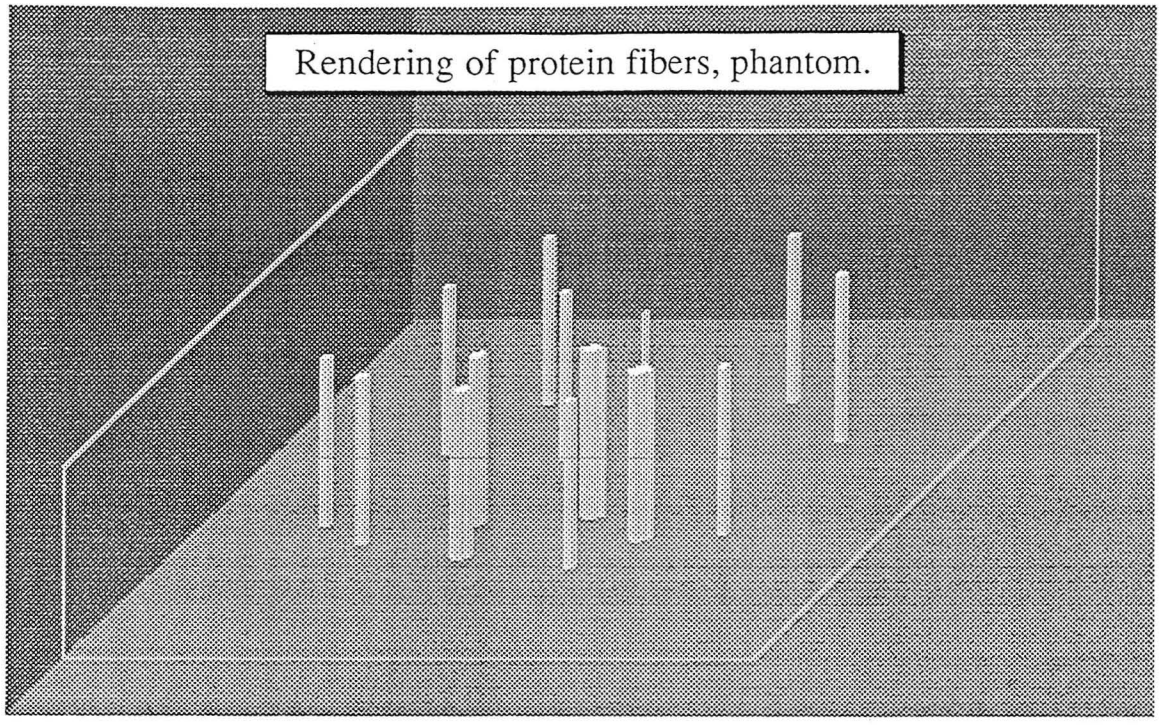

Figure 6

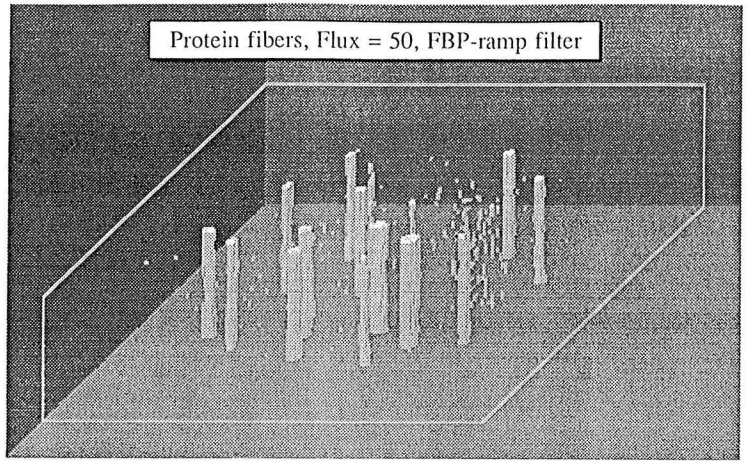

A)

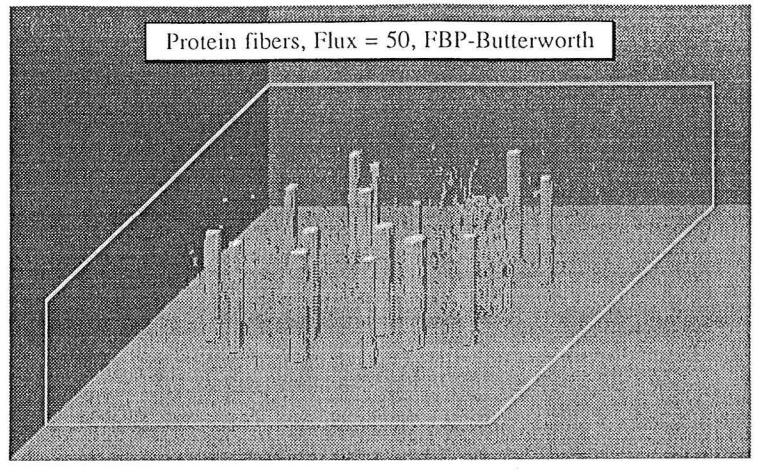

B)

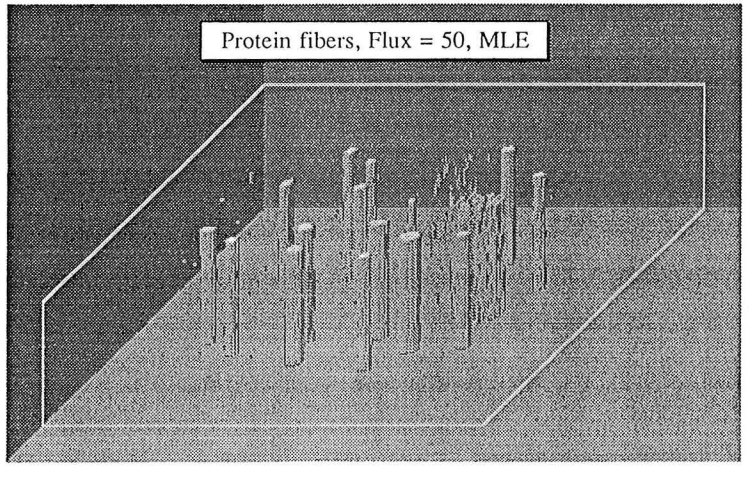

C)

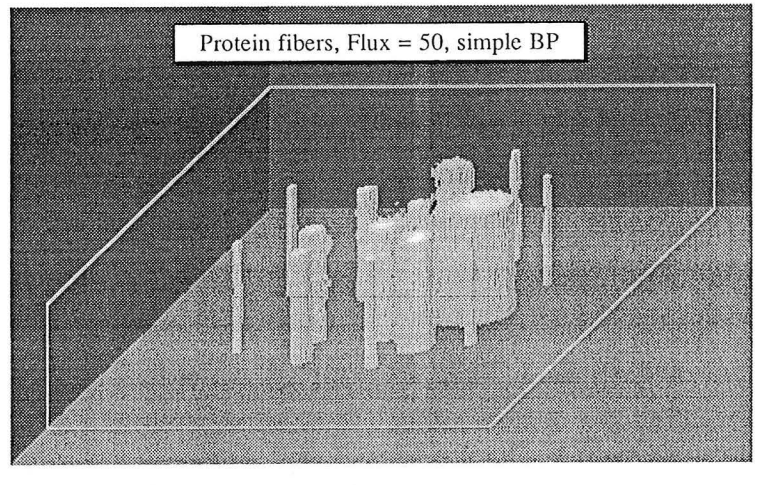

D)

Figure 7

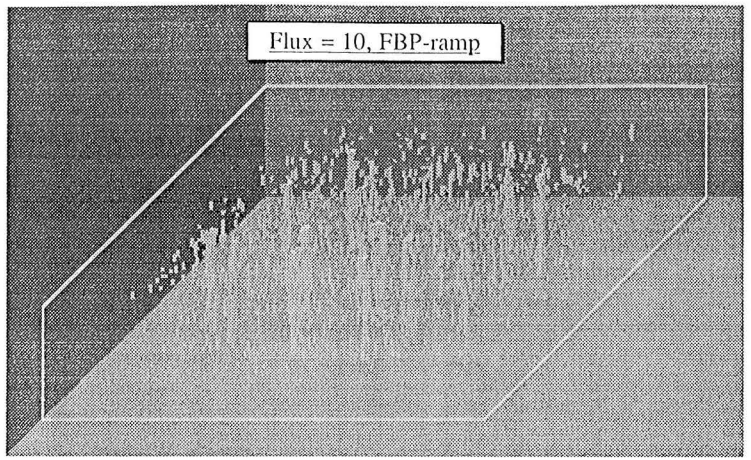

A)

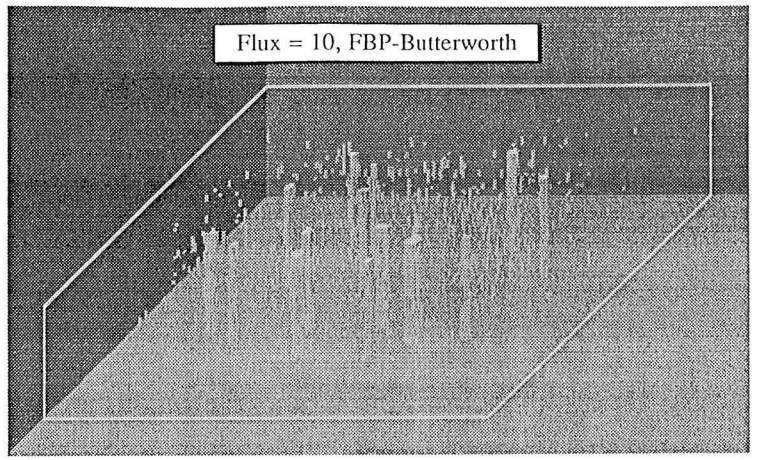

B)

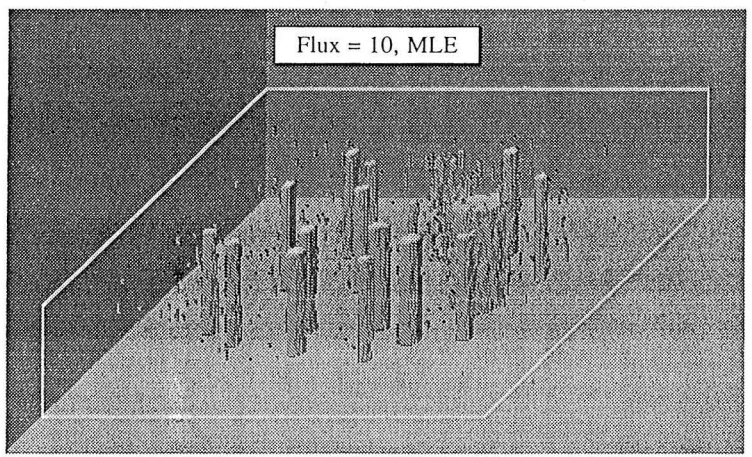

C)

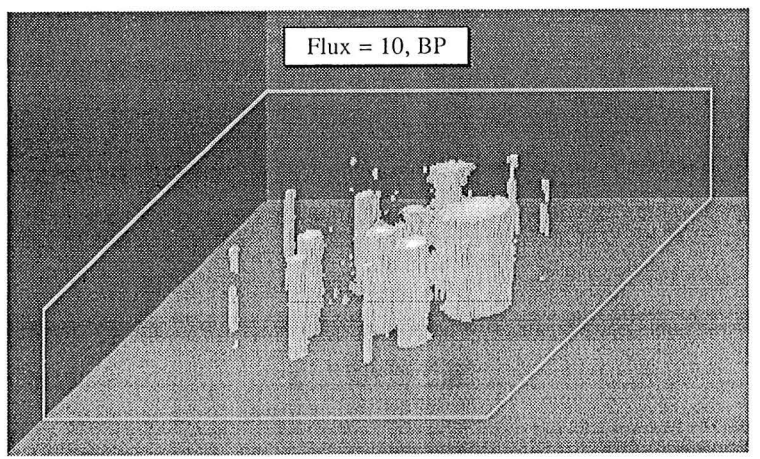

D)

Figure 8

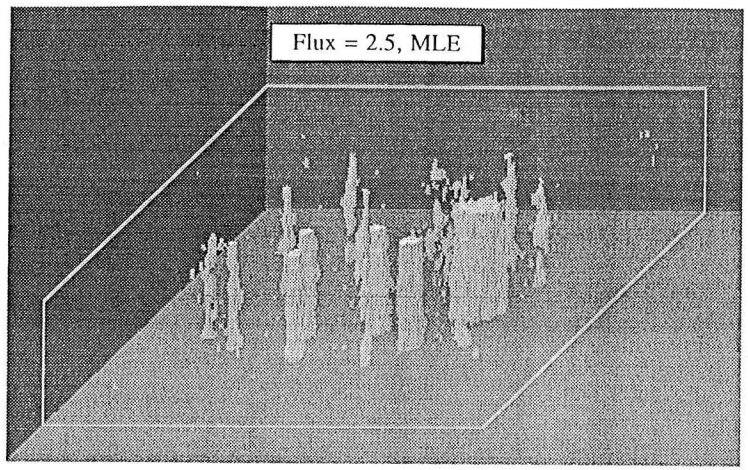

A)

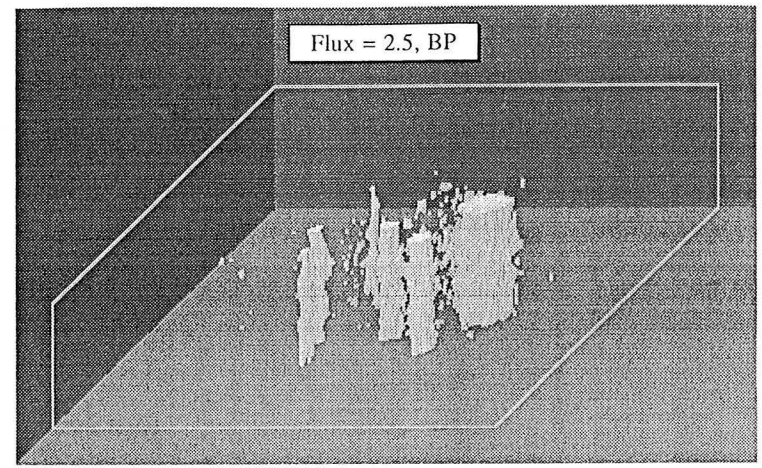

B)

Figure 9

LAWRENCE BERKELEY LABORATORY
UNIVERSITY OF CALIFORNIA
TECHNICAL INFORMATION DEPARTMENT
BERKELEY, CALIFORNIA 94720